

RSHazeDiff: A Unified Fourier-aware Diffusion Model for Remote Sensing Image Dehazing

Jiamei Xiong, Xuefeng Yan, Yongzhen Wang, Wei Zhao, Xiao-Ping Zhang, *Fellow, IEEE*, and Mingqiang Wei, *Senior Member, IEEE*

Abstract—Haze severely degrades the visual quality of remote sensing images and hampers the performance of automotive navigation, intelligent monitoring, and urban management. The emerging denoising diffusion probabilistic model (DDPM) exhibits the significant potential for dense haze removal with its strong generation ability. Since remote sensing images contain extensive small-scale texture structures, it is important to effectively restore image details from hazy images. However, current wisdom of DDPM fails to preserve image details and color fidelity well, limiting its dehazing capacity for remote sensing images. In this paper, we propose a novel unified Fourier-aware diffusion model for remote sensing image dehazing, termed RSHazeDiff. From a new perspective, RSHazeDiff explores the conditional DDPM to improve image quality in dense hazy scenarios, and it makes three key contributions. First, RSHazeDiff refines the training phase of diffusion process by performing noise estimation and reconstruction constraints in a coarse-to-fine fashion. Thus, it remedies the unpleasing results caused by the simple noise estimation constraint in DDPM. Second, by taking the frequency information as important prior knowledge during iterative sampling steps, RSHazeDiff can preserve more texture details and color fidelity in dehazed images. Third, we design a global compensated learning module to utilize the Fourier transform to capture the global dependency features of input images, which can effectively mitigate the effects of boundary artifacts when processing fixed-size patches. Experiments on both synthetic and real-world benchmarks validate the favorable performance of RSHazeDiff over multiple state-of-the-art methods. Source code will be released at <https://github.com/jm-xiong/RSHazeDiff>

Index Terms—RSHazeDiff, image dehazing, unified diffusion model, Fourier-aware refinement, phased training strategy

I. INTRODUCTION

REMOTE sensing (RS) images captured under hazy environments suffer from significant quality degradation, resulting in the performance deterioration of subsequent high-level tasks (e.g., image segmentation [1], road recognition [2]). Therefore, image dehazing is a necessary preprocessing step to promote the robustness of RS applications.

As image dehazing is a typical ill-posed problem, early works develop various prior assumptions to generate haze-free images [3]–[9]. These hand-crafted prior assumptions aim

to regularize the solution space of linear inverse problems. The well-known prior knowledge contains the dark channel prior (DCP) [3] and color attenuation prior (CAP) [4]. These methods effectively improve the overall visual quality of degraded images. However, predefined prior assumptions are only applied in specific scenarios, leading to severe color shift and undesired artifacts in practice.

Recently, various learning-based dehazing approaches have been proposed, and they may outperform prior-based methods. Specifically, early efforts [10]–[12] exploit convolutional neural networks (CNNs) to estimate the transmission maps or the airlight, and then generate sharp images via atmospheric scattering model (ASM) [13]. However, the cumulative error and unreliable prior assumptions often cause color distortions or haze residuals. Since then, considerable end-to-end dehazing approaches [14]–[19] focus on directly generating haze-free images from the corresponding hazy images. With the advantage of generative models, most dehazing methods based on generative adversarial networks (GANs) [20]–[25] regularize data distribution of dehazed images for haze removal. However, the training of GANs is unstable and susceptible to mode corruption, so GAN-based algorithms fail to achieve promising dehazing results.

Diffusion model is an emerging generative paradigm and successful in various low-level vision tasks [26]–[29]. With the superior modeling data distribution ability, diffusion models have achieved impressive performance in image generation. Moreover, the diffusion model is not subjected to unstable training and mode-collapse as GAN-based methods. Motivated by the strong generation ability of diffusion models, we leverage the conditional DDPM [30] for remote sensing image dehazing (RSID). However, there still exist several problems that limit the dehazing performance of DDPM. First, DDPM only uses simple noise-estimation constraints to optimize the network while ignoring image-level refinement. That simple constraining noise may introduce chaotic content and undesired impurity into restored images. Second, DDPM cannot utilize the potential structure and statistical information in the forward iterative process, limiting its better sampling capacity. In early sampling steps, the images captured in thick hazy scenarios make it difficult to complement the structure and color features, whereas the forward iterative process preserves relatively well-established information. By exploiting the beneficial information in the forward iterative, DDPM can better recover image details and color information (see Fig. 1(d)). Third, although the patch-based DDPM enables size-agnostic processing and sampling acceleration, it

Jiamei Xiong, Xuefeng Yan, Wei Zhao and Mingqiang Wei are with the School of Computer Science and Technology, Nanjing University of Aeronautics and Astronautics, Nanjing 210016, China, also with the Collaborative Innovation Center of Novel Software Technology and Industrialization, Nanjing 210093, China (e-mail: jmxiong@nuaa.edu.cn, yxf@nuaa.edu.cn, weizhao0120@nuaa.edu.cn, mingqiang.wei@gmail.com).

Yongzhen Wang is with the College of Computer Science and Technology, Anhui University of Technology, Ma'anshan 243099, China (e-mail: wangyz@ahut.edu.cn).

Xiao-Ping Zhang is with the Tsinghua Shenzhen International Graduate School, Tsinghua University, Shenzhen, China. (e-mail: xpzhang@ieec.org).



Fig. 1. Impact of different components in RSHazeDiff. From (a) to (f): (a) the hazy image, and the dehazing results of (b) Patch-based DDPM model, (c) Patch-based DDPM model with PTS, (d) Patch-based DDPM model with PTS and FIR module, (e) our full model (Patch-based DDPM model + PTS + FIR + GCL), and (f) the ground-truth image. PTS, FIR and GCL refer to the phased training strategy, Fourier-aware iterative refinement module and global compensated learning module, respectively.

yields evident block artifacts in that the patch-based strategy overlooks the global semantics of all patches. As shown in Fig. 1(e), introducing the global compensation learning module is beneficial to eliminate boundary artifacts and produce more visually pleasing images.

To overcome the aforementioned limitations, we propose a novel DDPM-based network for RSID, termed RSHazeDiff. Specifically, we regard the conditional DDPM as the basic architecture. Similar to the existing conditional strategy, RSHazeDiff adopts the degraded images as conditions to provide effective distribution guidance in the sampling process, preventing content diversity with the stochastic sampling process. In addition, we develop a phased training strategy (PTS) to effectively remedy the unsatisfactory results caused by simple noise-estimation constraint in the training phase. Concretely, we first train the diffusion model with the noise-estimation constraint, and then further optimize it with the reconstruction constraint. The reconstruction constraint aims to constrain the sampled restored results with its corresponding ground-truth images. Furthermore, to take advantage of latent structure and statistical information in the forward iterative process, we design a Fourier-aware iterative refinement (FIR) module. In each sampling step, FIR excavates the style/semantic information from the amplitude/phase components in Fourier domain for finer sampling results. Referring to the patch-based image processing in [31], we leverage the patch-based image processing strategy to ensure unlimited-size image dehazing. Nevertheless, separately dealing with each patch may ignore the global dependency features of all patches, leading to evident artifacts in the final result. In view of this, we utilize a global compensated learning module (GCL) to capture global dependency features and then incorporate GCL and local reverse denoising process into a unified format to produce high-quality output. Comprehensive experiments verify the superiority of RSHazeDiff on both synthetic and real-world RS hazy images, especially in dense hazy scenes.

Overall, our contributions are three-fold:

- A novel unified Fourier-aware conditional diffusion model is proposed for RSID (termed RSHazeDiff). It is a new exploration that applies diffusion models to RSID. RSHazeDiff leverages a phased training strategy

to address the content inconsistency caused by the simple noise-estimation constraint, which is beneficial to produce more satisfactory dehazing results.

- The Fourier-aware iterative refinement module is designed to further explore effective semantic and color information in the forward iterative process, better facilitating RSHazeDiff to preserve more texture details and color fidelity in restored images.
- The global compensated learning (GCL) module is introduced to eliminate evident block artifacts resulting from the patch-based image processing scheme. GCL can capture the global dependency features in RS images to assure the semantic consistency of all patches.

The remainder of this work is organized as follows. Section II presents the reviews of related work. Section III describes the preliminaries of the conditional DDPM. In Section IV, we introduce the general framework of RSHazeDiff and its details. Experimental results are presented and analyzed in Section V, followed by the conclusion in Section VI.

II. RELATED WORK

This section briefly reviews RSID algorithms and the diffusion model for image restoration. Existing RSID algorithms are classified into two categories: prior-based methods and learning-based methods.

A. Remote Sensing Image Dehazing

Prior-based methods. These methods [5]–[9] employ the hand-crafted priors to restore the dehazed images. For instance, Li *et al.* [5] develop a homomorphic filtering and sphere model improved DCP for nonhomogeneous haze and thin cloud removal. Xu *et al.* [6] design an iterative dehazing method named IDeRS, which introduces the concept of “virtual depth” for evaluating Earth surface coverings. Shen *et al.* [7] propose a spatial-spectral adaptive method for RSID, which corrects the ambient light and transmission estimation from the spatial and spectral dimensions. Han *et al.* [9] can effectively remove the haze of RS hazy images by exploiting multiscale guided filtering to decompose the input images into base layers and detail layers for final output. Although these

prior-based methods achieve impressive results, they rely on prior assumptions in specific scenes, making the dehazing results easily violated when the assumptions are not satisfied.

Learning-based methods. With the success of deep learning, researchers have focused on learning-based RSID algorithms [18], [19], [25], [32]–[36]. Similar to natural image dehazing, some RSID methods explore deep neural networks to estimate haze parameters in ASM. For example, Chi *et al.* [35] develop a trinity model called Trinity-Net to incorporate prior knowledge into the gradient-guided Swin Transformer [37] for haze parameters estimation. The other works directly convert hazy images to haze-free images in an end-to-end manner. Among them, Li and Chen [18] design a coarse-to-fine dehazing network called FCTF-Net, in which the first stage exploits an encoder–decoder architecture to obtain coarse dehazing results and then refines them in second stage. Zhang and Wang [19] propose a dynamic collaborative inference learning framework (DCIL) to handle haze removal of dense RS hazy images. Zheng *et al.* [25] exploit an enhanced attention-guide GAN-based network named Dehaze-AGGAN to restore haze-free remote sensing images in an unsupervised manner. However, few works focus on applying the diffusion model to image dehazing task, whereas the advanced generation ability of diffusion model makes it possible to better recover haze-free images.

B. Diffusion Models for Image Restoration

Diffusion-based generative models [30], [38], [39] progressively corrupt images by adding noise, and iteratively denoise from a noise distribution to a sharp image. With the superior generative capability, diffusion-based models have achieved remarkable performance in image restoration, such as image super-resolution [26], inpainting [27], shadow removal [28] and deblurring [29]. Saharia *et al.* [26] utilize conditional diffusion model for image super-resolution and achieve more competitive results than GAN-based methods. With similar condition strategy, Saharia *et al.* [27] propose a unified framework to handle image-to-image translation tasks by incorporating distorted images as the condition input. Rombach *et al.* [40] apply diffusion models in latent space to improve sampling efficiency. Considering that current diffusion model architectures mainly focus on fixed-sized image restoration, Ozan *et al.* [31] propose a patch-based diffusion model for unlimited-size image restoration. However, it fails to capture global information when operating locally on fixed-sized patches, which yields apparent block artifacts. To address this issue, we design a global compensated learning module to capture long-range context in frequency domain.

C. Fourier Transform in Deep Learning

Recently, the frequency information extracted through Fourier transform has attracted increasing attention in deep learning. A line of works utilizes it to improve representation ability of neural networks [41]–[44]. Among them, Xu *et al.* [41] demonstrate that the learning in frequency domain facilitates neural networks more efficiently and effectively. Wang *et al.* [43] reveal the relationship between the generalization of

CNNs and the high-frequency components of images. Besides, Zhou *et al.* [44] propose deep Fourier up-sampling for multi-scale modeling, which achieves impressive performance on multiple computer vision tasks in a plug-and-play manner. The other line of work applies the Fourier transform on many computer vision tasks [45]–[48]. For instance, Yang *et al.* [45] develop an effective phase consistency constraint to align source-target domains flexibly for domain adaptation semantic segmentation. Fuoli *et al.* [47] adopt Fourier domain losses to better recover the high-frequency content in image super-resolution. Yu *et al.* [48] explore the haze degradation property from a frequency domain perspective, and have achieved success in image dehazing by this property. However, no works attempt to exploit the potential of the Fourier spectral components in diffusion models. To our knowledge, we are the first to take the Fourier spectral components as important prior knowledge during iterative sampling steps of diffusion model, better preserving image details and colors.

III. PRELIMINARIES

DDPM originates the diffusion model [38], which defines two essential processes, i.e., the forward/diffusion process and reverse/denoising process. For the conditional DDPM [26], the degraded image is incorporated into the diffusion model as condition. With the guidance of conditional input, the diffusion model can pull the data distribution of restored images to conditional content distribution, preventing the content disparity caused by stochastic sampled noise. Next, we concisely introduce the conditional DDPM.

The diffusion process. The forward process gradually converts a clear data x_0 into a Gaussian noise distribution by T iterations. For any iteration, the corresponding transformation is depicted as:

$$q(x_t | x_{t-1}) = \mathcal{N}(x_t; \sqrt{1 - \beta_t}x_{t-1}, \beta_t I) \quad (1)$$

where β_t is the predefined variance schedule at the time step t , x_t represents the noisy image, and \mathcal{N} defines the Gaussian distribution. According to the property of the Markov chain, the above equation can be written in closed form:

$$\begin{aligned} q(x_t | x_0) &= \mathcal{N}(x_t; \sqrt{\bar{a}_t}x_0, (1 - \bar{a}_t) I) \\ &= \sqrt{\bar{a}_t}x_0 + \sqrt{1 - \bar{a}_t}\epsilon_t \end{aligned} \quad (2)$$

where $\bar{a}_t = \prod_{i=1}^t (1 - \beta_i)$, and $\epsilon_t \sim \mathcal{N}(0, \mathbf{I})$ with the same dimensionality as x_t . When total step T is large enough, x_t follows a standard Gaussian distribution.

The denoising process. The reverse process is designed to reconstruct the desired data samples from the Gaussian noise by progressively denoising based on Markov chain. Each denoising step of the reverse process can be described as:

$$p_0(x_{t-1} | x_t, \bar{x}) = \mathcal{N}(x_{t-1}; u_0(x_t, \bar{x}, t), \sigma_t^2 I) \quad (4)$$

where the invariant variance $\sigma_t^2 = \frac{1 - \bar{a}_{t-1}}{1 - \bar{a}_t} \beta_t$, the learned mean $u_0(x_t, \bar{x}, t) = \frac{1}{\sqrt{\bar{a}_t}} \left(x_t - \frac{1 - \bar{a}_t}{\sqrt{1 - \bar{a}_t}} \epsilon_0(x_t, \bar{x}, t) \right)$, and \bar{x} defines the conditional image. In Eq. 4, the $\epsilon_0(x_t, \bar{x}, t)$ is only variable and usually predicted by a denoising U-net network [49]. To

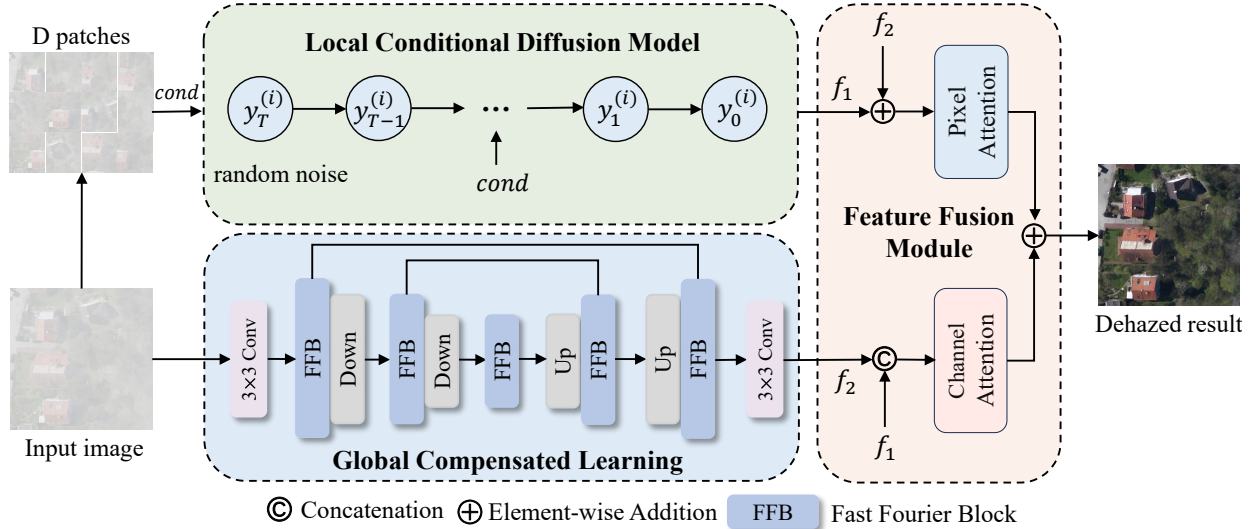


Fig. 2. The overall architecture of RSHazeDiff for RSID. RSHazeDiff contains a local reverse denoising process, a global compensated learning module, and a feature fusion module. The local reverse denoising process focuses on locally sampling over patches, while GCL module performs the intact images with global properties in Fourier domain. Then, the global-local feature representations are fused by the feature fusion module to produce final dehazed images. We decompose an input image into D overlapping fixed-sized patches via [31]. *cond* means that the D patches are regarded as the conditions of local reverse denoising process. $y_t^{(i)}$ defines the i -th patch of the noisy image y_t that gradually samples from the random noise patch $y_T^{(i)}$ to the haze-free patch $y_0^{(i)}$ by t iterations. f_1 and f_2 represent the output of local reverse denoising process and GCL module, respectively.

approximate this value, the learned model is optimized by following training objective:

$$\mathcal{L}_{noise} = E_{x_0, \bar{x}, t, \epsilon_t} \left[\left\| \epsilon_t - \epsilon_0 \left(\sqrt{a_t} x_0 + \sqrt{1 - a_t} \epsilon_t, \bar{x}, t \right) \right\|^2 \right] \quad (5)$$

IV. METHODOLOGY

We rethink RSID from the perspective of diffusion model. RSHazeDiff exploits the conditional DDPM to produce dehazing results with closer distribution to the clear data. Specifically, to eliminate that simple noise estimation produces unsatisfactory content in dehazing result, we leverage the reconstruction constraint to further optimize DDPM. Moreover, we explore the effective semantic and color information in the forward iterative process, better helping RSHazeDiff to preserve more texture details and color fidelity in sampled restoration results. Considering that patch-based image processing strategy cannot effectively capture global dependency features, we introduce a global compensated learning module to capture long-range context by executing simple yet effective spectrum transform in frequency domain.

In this section, we first describe the overview of RSHazeDiff. After that, the designed Fourier-aware iterative refinement and global compensated learning modules are elaborated in detail. Finally, we present the phased training strategy applied in the proposed method.

A. Overview

Fig. 2 illustrates the overall architecture of RSHazeDiff, which consists of three main components: a local reverse denoising process, a global compensated learning module, and a feature fusion module. The local reverse denoising process

leverages the Fourier-aware condition diffusion model to perform local patch-level restoration, and an input hazy image is randomly cropped with several patches as its conditions. The detailed training and sampling process of Fourier-aware conditional diffusion model is exhibited in Fig. 3, and its pseudocodes are depicted in Alg. 1 and Alg. 2. Note that we crop the whole image into overlapping patches as the input of Fourier-aware conditional diffusion model by using the grid-like arranged parsing scheme [31]. In turn, we merge all patches with the dictionary of their locations and adopt the mean estimated noise for overlapping pixels [31] (lines 8,9,11 in Alg. 2). GCL module adopts the Fast Fourier Block (FFB) as the basic unit of U-net architecture to capture global feature representations. The structure of FFB is shown Fig. 4. Finally, the feature fusion module fuses the global-local feature representations to produce the final dehazing results.

B. Fourier-aware Iterative Refinement

DDPM-based image restoration approaches tend to tackle the forward diffusion process and reverse denoising process in sequence. The reverse process progressively sample with variable $\epsilon_0(x_t, \bar{x}, t)$ predicted in the forward process. Apart from that, the two processes are independent to a certain extent. Nevertheless, each iteration in the forward process can provide beneficial guided features to the sampling process. As depicted in [50], the amplitude and phase components in Fourier space correspond to low-level statistics and high-level semantic information of input images. This characteristic can be extended in image dehazing task. The amplitude spectrum contains more hazy degradation properties (e.g., illumination and contrast), while the phase spectrum preserves more texture structure of images. In early sampling steps, dense hazy images suffer from severe structure and color information

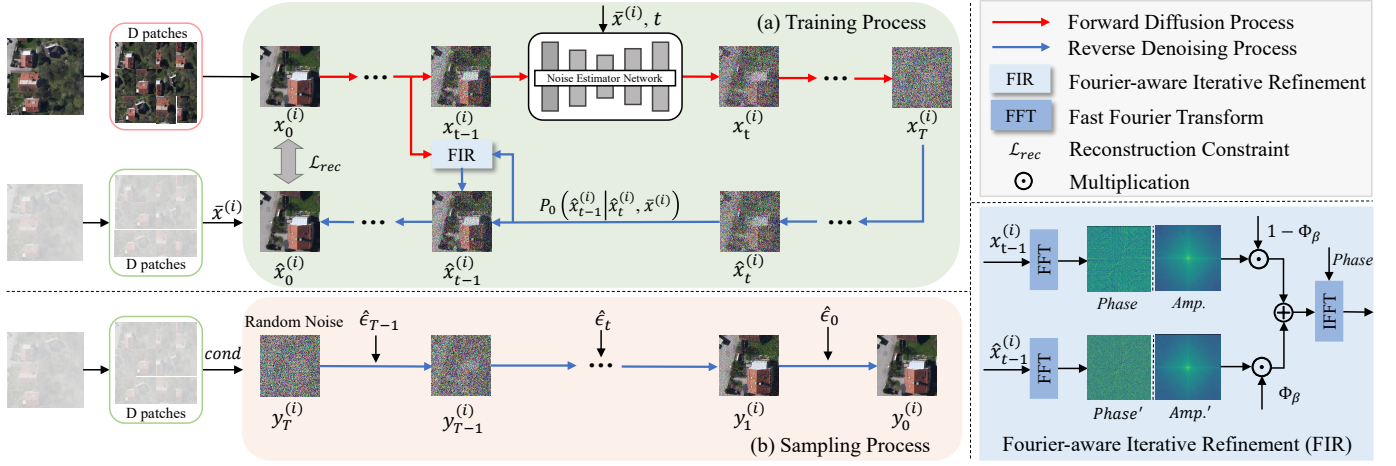


Fig. 3. The architecture of the Fourier-aware conditional diffusion model, which contains two processes: (a) The training process adopts the phased training strategy to produce finer dehazing results. The model is first optimized with noise estimation constraint, and then the coarse sampling result by reverse denoising process is refined with reconstruction constraint. Also, the well-designed FIR excavates the structure and color guided representation from the forward process in Fourier space for finer sampling results. (b) The sampling process intends to gradually convert a Gaussian noise into the restored image. Note that the above model performs patch-level restoration.

Algorithm 1 The training process of Fourier-aware conditional diffusion model

Input: Clean image x_0 , hazy image conditioner \bar{x} , denoiser network $\epsilon_\theta(x_t, \bar{x}, t)$, a random binary patch mask \mathbf{P}_i , transitional iteration M , number of implicit sampling steps S , time steps T , and the mask Φ_β in FIR module.

```

1: while Not converged do
2:    $x_0^{(i)} = \text{Crop}(\mathbf{P}_i \circ x_0)$  and  $\bar{x}^{(i)} = \text{Crop}(\mathbf{P}_i \circ \bar{x})$ 
3:    $t \sim \text{Uniform}\{1, \dots, T\}$ 
4:    $\epsilon_t \sim \mathcal{N}(\mathbf{0}, \mathbf{I})$ 
5:   if Current iterations  $\leq M$  then
6:     Take gradient descent step on
7:     
$$\nabla_\theta \left\| \epsilon_t - \epsilon_0 \left( \sqrt{\bar{\alpha}_t} x_0^{(i)} + \sqrt{1 - \bar{\alpha}_t} \epsilon_t, \bar{x}^{(i)}, t \right) \right\|^2$$

8:   else
9:      $\hat{x}_{t_S}^{(i)} \sim \mathcal{N}(\mathbf{0}, \mathbf{I})$ 
10:    for  $j = S : 1$  do
11:       $t = (j - 1) \cdot T/S + 1$ 
12:       $t_{next} = (j - 2) \cdot T/S + 1$  if  $j > 1$  else 0
13:       $\hat{\epsilon}_t = \epsilon_\theta(\hat{x}_t^{(i)}, \bar{x}^{(i)}, t)$ 
14:       $x_{t_{next}}^{(i)} = \sqrt{\bar{\alpha}_{t_{next}}} x_0^{(i)} + \sqrt{1 - \bar{\alpha}_{t_{next}}} \hat{\epsilon}_{t_{next}}$ 
15:       $\hat{x}_{t_{next}}^{(i)} = \sqrt{\bar{\alpha}_{t_{next}}} \left( \frac{\hat{x}_t^{(i)} - \sqrt{1 - \bar{\alpha}_t} \hat{\epsilon}_t}{\sqrt{\bar{\alpha}_t}} \right) + \sqrt{1 - \bar{\alpha}_{t_{next}}} \cdot \hat{\epsilon}_t$ 
16:       $\hat{x}_{t_{next}}^{(i)} = \text{FIR} \left( x_{t_{next}}^{(i)}, \hat{x}_{t_{next}}^{(i)}, \Phi_\beta \right)$ 
17:    end for
18:    Take gradient descent step on  $\nabla_\theta \mathcal{L}_{rec} \left( \hat{x}_0^{(i)}, x_0^{(i)} \right)$ 
19:  end if
20: end while
21: return  $\theta$ 
    
```

loss, whereas the forward iterative process preserves pretty well-established information. Inspired by that, we design a Fourier-aware iterative refinement module, which excavates the structure and color guided representation from the forward

Algorithm 2 The sampling process of Fourier-aware conditional diffusion model

Input: Hazy image \bar{x} , $\epsilon_\theta(y_t, \bar{x}, t)$, S , T , and dictionary of D overlapping patch locations.

```

1:  $y_{t_S} \sim \mathcal{N}(\mathbf{0}, \mathbf{I})$ 
2: for  $j = S : 1$  do
3:    $t = (j - 1) \cdot T/(S - 1) + 1$ 
4:    $t_{next} = (j - 2) \cdot T/(S - 1) + 1$  if  $j > 1$  else 0
5:    $\hat{\Omega}_t = \mathbf{0}$  and  $\mathbf{M} = \mathbf{0}$ 
6:   for  $d = 1 : D$  do
7:      $y_t^{(d)} = \text{Crop}(\mathbf{P}_d \circ y_t)$  and  $\bar{x}^{(d)} = \text{Crop}(\mathbf{P}_d \circ \bar{x})$ 
8:      $\hat{\Omega}_t = \hat{\Omega}_t + \mathbf{P}_d \cdot \epsilon_\theta(y_t^{(d)}, \bar{x}^{(d)}, t)$ 
9:      $\mathbf{M} = \mathbf{M} + \mathbf{P}_d$ 
10:  end for
11:   $\hat{\Omega}_t = \hat{\Omega}_t \oslash \mathbf{M}$  //  $\oslash$ : element-wise division
12:   $y_{next} = \sqrt{\bar{\alpha}_{t_{next}}} \left( \frac{y_t - \sqrt{1 - \bar{\alpha}_t} \cdot \hat{\Omega}_t}{\sqrt{\bar{\alpha}_t}} \right) + \sqrt{1 - \bar{\alpha}_{t_{next}}} \cdot \hat{\Omega}_t$ 
13: end for
14: return  $y_0$ 
    
```

process in Fourier domain to refine each transition of sampling process. The well-designed FIR module can help diffusion model to generate more natural and realistic images.

The detailed structure of FIR is illustrated in Fig. 3. Note that the $x_0^{(i)}$ represents i -th patch cropped from the clear image x_0 . we first transition step from a patch $x_{t-1}^{(i)}$ to $x_t^{(i)}$ through Eq. 1, and then sample from $\hat{x}_t^{(i)}$ to $\hat{x}_{t-1}^{(i)}$ through Eq. 4. Then, images $x_{t-1}^{(i)}$ and $\hat{x}_{t-1}^{(i)}$ are decomposed to amplitude and phase components in Fourier domain by Fast Fourier Transform (FFT) [51]. Next, we use the phase spectrum of $x_{t-1}^{(i)}$ and integrate the partial amplitude spectrum of $x_{t-1}^{(i)}$ into amplitude component of $\hat{x}_{t-1}^{(i)}$. Finally, we apply the inverse Fast Fourier Transform (IFFT) to transform the final fused results $\hat{x}_{t-1}^{(i)}$ back to spatial domain image. Given a single channel image $x \in \mathcal{R}^{H \times W}$, its Fourier transform \mathcal{F} as a complex component

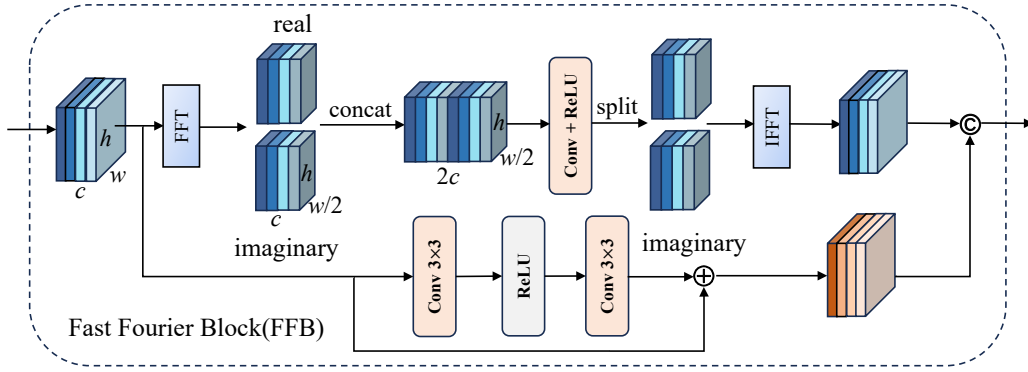


Fig. 4. The detailed structure of the fast Fourier block, which can capture the long-range context by executing simple yet effective spectrum transform.

can be expressed as:

$$\mathcal{F}(x)(m, n) = \frac{1}{\sqrt{HW}} \sum_{h=0}^{H-1} \sum_{w=0}^{W-1} x(h, w) e^{-j^{2\pi} \left(\frac{h}{H}m + \frac{w}{W}n \right)} \quad (6)$$

here m, n define the coordinates in Fourier space, and $j^2 = -1$. For an RGB image, each channel is adopted the Fourier transform separately. The amplitude component $\mathcal{A}(x)$ and phase component $\mathcal{P}(x)$ can be computed as:

$$\mathcal{A}(x)(m, n) = \sqrt{R^2(x)(m, n) + I^2(x)(m, n)} \quad (7)$$

$$\mathcal{P}(x)(m, n) = \arctan \left[\frac{I(x)(m, n)}{R(x)(m, n)} \right] \quad (8)$$

where $R(x)$ and $I(x)$ are the real and imaginary parts of the complex component. Therefore, every reverse step can be formalized as follows:

$$\hat{x}_{t-1}^{(i)} = \mathcal{F}^{-1} \left(\Phi_{\beta} \mathcal{A} \left(\hat{x}_{t-1}^{(i)} \right) + (1 - \Phi_{\beta}) \mathcal{A} \left(x_{t-1}^{(i)} \right), \mathcal{P} \left(x_{t-1}^{(i)} \right) \right) \quad (9)$$

where $\hat{x}_{t-1}^{(i)} = \text{Crop}(\mathbf{P}_i \circ \hat{x}_{t-1})$ and $x_{t-1}^{(i)} = \text{Crop}(\mathbf{P}_i \circ x_{t-1})$ define i -th $p \times p$ patch from image pair (\hat{x}_{t-1}, x_{t-1}) . The $\text{Crop}(\circ)$ operation extracts the patch from the location \mathbf{P}_i within the complete image. \mathcal{F}^{-1} defines inverse Fourier transform. Similar to [46], Φ_{β} represents an image mask that only the value of a small center region is non-zero. The small center area is $[-\beta H : \beta H, -\beta W : \beta W]$. The coordinates of the center in the images are set $(0, 0)$ and $\beta \in (0, 1)$.

By fully exploiting the unexplored texture structure and color information in forward iterative process, FIR module can refine DDPM to generate more visually pleasing images. The relevant experiments in Section V-D show that dehazing performance is improved with the use of the FIR.

C. Global Compensated Learning

It is significant that the image restoration methods can handle unlimited-size images in practice. To achieve unlimited-size image restoration, we adopt the patch-based processing strategy that divides images into multiple fixed-size patches and then deals with each patch independently. However, this patch-based strategy may produce artifacts with the ignorance of global dependency information in all patches. To address this, we propose an effective GCL module that adopts FFB

as the basic U-net architecture unit to capture all patches' global dependency information. After learning global feature representations, the designed fusion module fuses the local patch-based image restoration process and GCL module in a pixel-channel attention collaborative manner. The detailed structure of GCL module and the fusion module are illustrated in Fig. 2.

In GCL, we apply FFB to deal with the entire images based on the spectral convolution theorem [52], which observes that updating each pixel value in spectral space affects all spatial pixels (i.e., Fourier domain embraces global properties). As illustrated in Fig. 4, FFB employs the 1×1 convolution operator to tackle real and imaginary parts in Fourier space for capturing frequency representations, while adopts a residual block with two 3×3 convolution layers for capturing spatial representations. After that, the final results are produced by concatenation and convolution operation. Therefore, the simple yet effective spectrum transform in the Fourier space can be used to capture the long-range context feature.

After capturing the global feature, we use a feature fusion module to fuse local patch-based denoising process and global compensated learning module. Referring to the statement in [53], only adopting addition or concatenation operations to fuse two feature maps is less effective. Hence, we introduce two parallel attention modules to further fuse features in a pixel-channel collaborative manner. The pixel attention (PA) [15] can produce a $1 \times H \times W$ attention map while the channel attention (CA) [15] produces a $C \times 1 \times 1$ attention map. The two attention modules can handle different types of information flexibly, i.e., haze pixels and more important channel information. Therefore, we adopt the element-wise addition operation between the local patch-based denoising process and GCL module before PA and the channel-wise concatenation operation before CA. Above all, the collaborative pixel-channel fusion is used to generate the final dehazing result. The fusion module can be described as follows:

$$\mathcal{F}_{out} = \mathcal{C} \left(\mathcal{C} \left(\mathcal{C} \left(\mathcal{C} \left(f_1 \right), \mathcal{C} \left(f_2 \right) \right) \right) + \mathcal{P} \mathcal{A} \left(\mathcal{C} \left(f_1 \right) + \mathcal{C} \left(f_2 \right) \right) \right) \quad (10)$$

where f_1 and f_2 are the output of local reverse denoising process and global compensated learning module, respectively. \mathcal{C} represents the convolution layer and $[\cdot]$ is the concatenation operation.

D. Phased Training Strategy

Simple constraining the training phase of diffusion model with noise estimation cannot effectively restore satisfactory results. That is because the noise-estimation constraint focuses on distribution-closer approximation, whereas narrowing the disparity between restored and clear data distribution cannot enable model to generate visually pleasing output. In view of this, we employ reconstruction constraint to refine the training phase to obtain finer result with realistic colors and rich details. Specifically, PTS optimizes DDPM by constraining the noise-estimation in the early stages. After that, a coarse restored image, obtained by performing the sampling algorithm in the training phase, is constrained with corresponding ground-truth ones for finer restored results. PTS refines unsatisfactory results caused by simple noise-estimation constraint.

The noise-estimation constraint is depicted in Eq. 5. The L_1 loss and multi-scale structural similarity loss (MS-SSIM) are adopted as the reconstruction constraint. Since [54] has proved that L_1 loss can provide better convergence and restoration performance than L_2 loss, we leverage L_1 loss to constrain the coarse restored results with ground-truth ones. The MS-SSIM loss ($\mathcal{L}_{ms-ssim}$) focuses on assessing the difference between the coarse restored results $\hat{x}_0^{(i)}$ and clear patch $x_0^{(i)}$ and its can be defined as follows:

$$\mathcal{L}_{ms-ssim} = 1 - \prod_{m=1}^M \left(\frac{2u_{\hat{x}_0^{(i)}}u_{x_0^{(i)}} + C_1}{u_{\hat{x}_0^{(i)}}^2 + u_{x_0^{(i)}}^2 + C_1} \right)^{\beta_m} \left(\frac{2\sigma_{\hat{x}_0^{(i)} \cdot x_0^{(i)}} + C_2}{\sigma_{\hat{x}_0^{(i)}}^2 + \sigma_{x_0^{(i)}}^2 + C_2} \right)^{\gamma_m} \quad (11)$$

here $u_{\hat{x}_0^{(i)}}$, $u_{x_0^{(i)}}$ and $\sigma_{\hat{x}_0^{(i)}}$, $\sigma_{x_0^{(i)}}$ define the mean and standard deviations of $\hat{x}_0^{(i)}$ and $x_0^{(i)}$, and $\sigma_{\hat{x}_0^{(i)} \cdot x_0^{(i)}}$ is their covariance. C_1 and C_2 are constants and usually set $C_1 = 0.0001$, $C_2 = 0.0009$, β_m and γ_m are the relative importance of two components and both set to 1. M represents the number of scales and we set it to five according to [55]. Therefore, the overall reconstruction constraint \mathcal{L}_{rec} during the late training stage is defined as:

$$\mathcal{L}_{rec} = \mathcal{L}_1 + \mathcal{L}_{ms-ssim} \quad (12)$$

In general, the conditional DDPM is trained by simple noise-estimation constraint (\mathcal{L}_{noise}) in the early stages, and then minimizes the reconstruction constraint (\mathcal{L}_1 and $\mathcal{L}_{ms-ssim}$) for finer training optimization. Note that these loss functions are locally operated on fixed-sized patches.

Apart from the above mentioned loss function that is optimized over local patch, we also exploit the perceptual loss to global compensated learning module for constraining the whole image. The perceptual loss function can measure high-level semantic/perceptual similarity between the output and ground truth by extracting the multi-layer features from pre-trained network VGG-19 [56]. By minimizing perceptual loss, the restored output f_2 has more similar texture and structure features with ground-truth images.

To be special, we hierarchically extract the latent feature maps from VGG-19 model to measure the image similarities

between the output f_2 and ground-truth images z , which can be expressed as:

$$\mathcal{L}_{perceptual} = \sum_{i=1}^5 \omega_i \|F_i(f_2) - F_i(z)\|_1 \quad (13)$$

where $F_i(\cdot)$ represents the i -th latent features obtained by the feature extraction network. ω_i denotes the weight coefficient of the i -th feature representation. Furthermore, we also employ pixel-level \mathcal{L}_1 loss to assess the diversity between f_2 and z . Hence, the loss function \mathcal{L}_{global} in global compensated learning branch is shown as:

$$\mathcal{L}_{global} = \mathcal{L}_1 + \mathcal{L}_{perceptual} \quad (14)$$

Overall, PTS enables diffusion model to effectively fine local details in patch-based manner. In addition, we employ perceptual loss to optimize the final result by narrowing the semantic disparity between restored results and ground-truth image. In this way, RSHazeDiff can learn global-local feature representations to produce visually more pleasing results.

V. EXPERIMENTS

In this section, the implementation details in our experiments are first described. Then, the comparisons with state-of-the-art approaches on the synthetic and real-world datasets are performed. Finally, we conduct ablation studies to demonstrate the effectiveness of core components in RSHazeDiff.

A. Implementation Details

Dataset. We evaluate the performance of RSHazeDiff on three RS hazy datasets, *i.e.*, the light hazy image dataset (LHID), the dense hazy image dataset (DHID) [19] and expanded remote sensing image cloud removing dataset (ERICE) [19]. LHID and DHID are two synthetic datasets with light and dense haze, and each image has 512×512 pixels. LHID contains 30,517 pairs of hazy RS images for training and 500 pairs for testing (*i.e.*, LHID-A or LHID-B). In our experiments, we merge LHID-A and LHID-B, and test networks on LHID with 1,000 image pairs. Based on the atmospheric scattering model, the ambient light $A \in [0.7, 1]$ and 500 different real-world transmission maps are randomly sampled to generate DHID dataset. DHID dataset contains 14,990 dense hazy images, with 14,490 for training and 500 for testing. The ERICE is a real-world dataset expanded on RICE1 [57], which are collected in some scene categories from Google Earth (*i.e.*, mountain, river, desert, snowberg, forest, farmland, residential). In ERICE dataset, 1,850 and 150 images are regarded as training and test sets, each with a resolution of 256×256 pixels.

Training Details. All experiments are implemented by PyTorch [58] framework with NVIDIA GeForce RTX 3090 GPU. In the training of Fourier-aware conditional diffusion model, we adopt the Adam optimizer and the initial learning rate of 0.00002. The batch and patch size are set as 4 and 64×64 . We adopt PTS to train the model until it converges. Concretely, we first train the model with noise estimation constraint for 1,500,000 iterations, and then refine it with reconstruction

TABLE I

QUANTITATIVE COMPARISONS (AVERAGE PSNR/SSIM/CIEDE2000) WITH 11 STATE-OF-THE-ART DEHAZING APPROACHES ON THE SYNTHETIC LHID AND DHID DATASETS. THE \uparrow MEANS HIGHER IS BETTER WHILE \downarrow MEANS LOWER IS BETTER. THE BEST RESULTS ARE WRITTEN IN **BOLDFACE**

Method	Publication	LHID			DHID		
		PSNR \uparrow	SSIM \uparrow	CIEDE2000 \downarrow	PSNR \uparrow	SSIM \uparrow	CIEDE2000 \downarrow
DCP [3]	TPAMI'10	21.12	0.818	9.161	18.92	0.824	9.867
AOD-Net [12]	ICCV'17	22.24	0.842	7.122	15.37	0.718	14.272
GridDehazeNet [14]	ICCV'19	26.64	0.883	4.597	25.51	0.868	5.053
IDeRs [6]	INS'19	14.68	0.627	19.563	13.33	0.575	19.942
FFA-Net [15]	AAAI'20	27.79	0.887	4.424	25.05	0.880	5.590
PSD [16]	CVPR'21	23.33	0.855	6.998	23.30	0.853	6.911
FCTF-Net [18]	GRSL'21	25.85	0.876	5.423	17.21	0.739	12.794
DCIL [19]	TGRS'22	28.12	0.898	5.180	26.95	0.896	4.877
Trinity-Net [35]	TGRS'23	24.78	0.867	6.737	25.86	0.878	5.479
Focal-Net [17]	ICCV'23	29.39	0.899	4.012	25.73	0.887	5.313
RSHazeDiff	Ours	29.65	0.905	3.875	27.91	0.900	3.945

constraint for 500,000 iterations in LHID. Similarly, we first train the model for 1,000,000 iterations and then refine it for 500,000 iterations in DHID. To expedite the sampling process, we adopt the implicit sampling strategy [59] in which the total number of time steps and implicit sampling steps are set to 1,000 and 10. Furthermore, we use the exponential moving average (EMA) strategy [60] to eliminate slight color shift problem. During the training of the global compensated learning module, we use the Adam optimizer with the batch size of 8 and the initial learning rate of 0.001.

Evaluation Settings. To demonstrate the superiority of RSHazeDiff, we qualitatively and quantitatively compare it against ten representative SOTA dehazing algorithms, including DCP [3], AOD-Net [12], GridDehazeNet [14], IDeRs [6], FFA [15], PSD [16], FCTF-Net [18], DCIL [19], Trinity-Net [35], and Focal-Net [17].

The three well-known full-referenced quantitative evaluation metrics Peak Signal to Noise Ratio (PSNR), Structural Similarity Index (SSIM) [61] and CIEDE2000 [62] are adopted for dehazing performance evaluation. PSNR index assesses the error between the dehazed images and the corresponding ground-truth ones pixel by pixel, while SSIM measures image similarity regarding brightness, contrast, and structure. Larger values of PSNR and SSIM indicate better results. CIEDE2000 indicator is employed to evaluate the color distinction between the dehazed image and its haze-free counterpart. A smaller value of CIEDE2000 indicates better performance.

B. Comparison with State-of-the-art Methods

Results on Synthetic Dataset. Table I reports the quantitative performance of eleven dehazing algorithms on synthetic LHID and DHID test datasets. To make fair comparisons, we re-train all compared methods on synthetic datasets according to the implementation details of their papers. Note that we directly re-train the whole network of DCIL on DHID dataset without the phased learning strategy [19]. As observed, our RSHazeDiff can achieve the highest PSNR and SSIM values and the lowest CIEDE2000 values than other representative SOTA dehazing algorithms, which indicates that our RSHazeDiff is able to better restore the texture details and color information from hazy RS images.

Fig. 5 presents the visual comparisons against several state-of-the-art dehazing approaches on DHID datasets. We can observe that AOD-Net tends to darken the whole images and produce noticeable Halo artifacts, degrading the overall visibility of the dehazed images. FFA-Net and Focal-Net cannot remove haze effectively when dealing with dense hazy images, leading to some haze residuals. In addition, the dehazing results of FFA-Net suffer from slight color distortion. Although DCIL can remove a majority of haze to a certain extent, it may distort some texture details of input images and fails to completely remove the haze in some regions. Trinity-Net cannot produce pleasing dehazing results due to haze residuals and serious color distortion. Compared with above SOTA algorithms, our RSHazeDiff can generate much clearer haze-free images with realistic color fidelity and finer texture details.

Results on Real-World Hazy Images. To further validate the generalization ability on real-world images, we evaluate our method against other state-of-the-art dehazing approaches on ERICE dataset. The ERICE dataset contains some images captured in thick haze scenarios. Table II exhibits the quantitative comparison results over eleven representative dehazing algorithms. As reported, the proposed method surpasses other dehazing algorithms in terms of PSNR and SSIM, indicating that the images restored by RSHazeDiff are most similar to its corresponding ground-truth images. Although CIEDE2000 value of RSHazeDiff is not the best, our method wins the second place among eleven competitive dehazing algorithms. The quantitative results verify that the superiority of RSHazeDiff on real-world RS images.

Fig. 6 presents four real-world hazy samples from ERICE and the corresponding dehazing results produced by different dehazing methods. As displayed, AOD-Net fails to produce visually pleasing images due to abundant haze residuals, especially in thick hazy scenarios. The dehazed images of FFA-Net and Focal-Net still remain residual haze and cannot restore clear texture details. Although the dehazing results produced by DCIL seem good, they suffer from slight color shift and contain residual haze in some regions. Trinity-Net fails to remove haze completely and may yield over-saturation in restored images. In contrast, our method succeeds

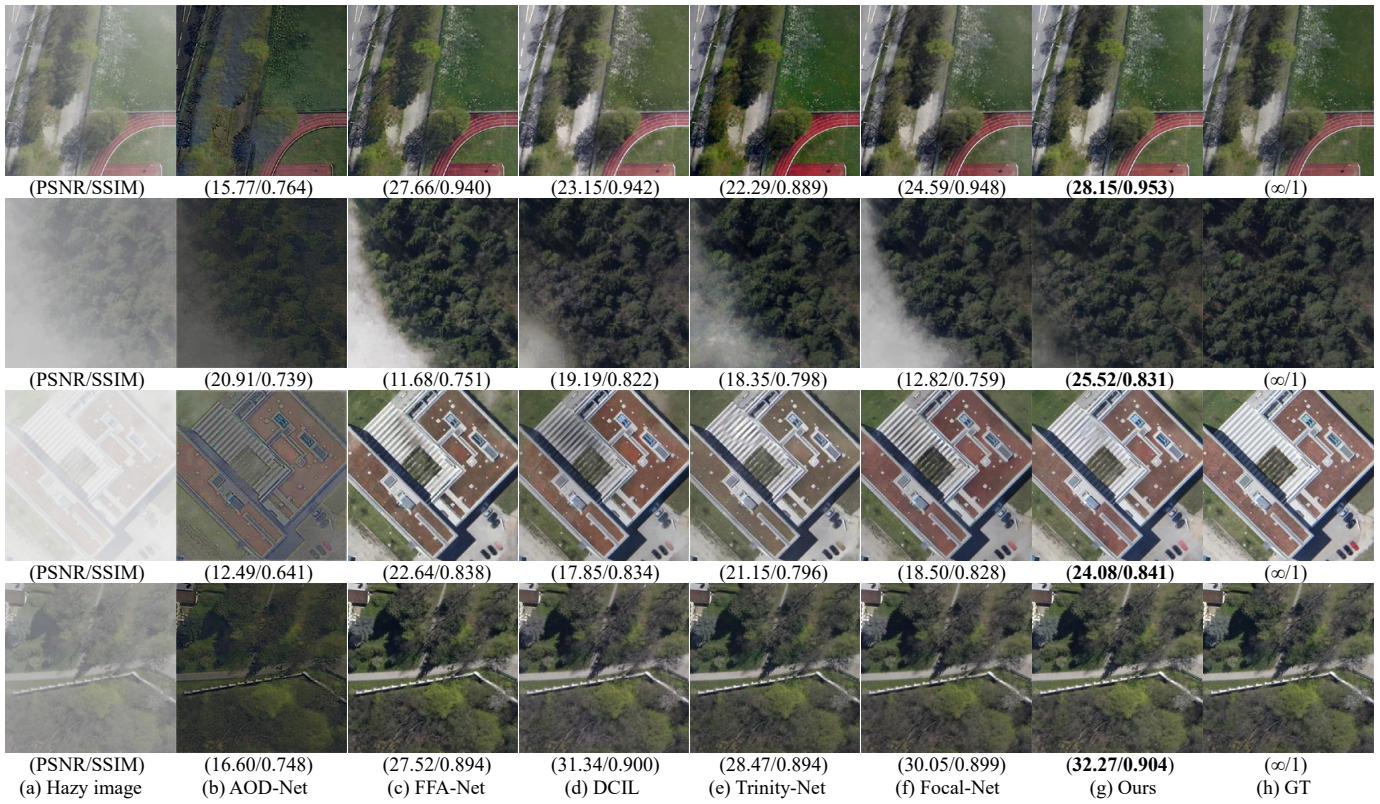


Fig. 5. Qualitative comparisons on DHID dataset. From (a) to (h): (a) the hazy image, and the dehazing results of (b) AOD-Net [12], (c) FFA-Net [15], (d) DCIL [19], (e) Trinity-Net [35], (f) Focal-Net [17], (g) our RSHazeDiff, respectively, and (h) the ground-truth image. As observed, our RSHazeDiff can generate much clearer haze-free images with well-preserved details.

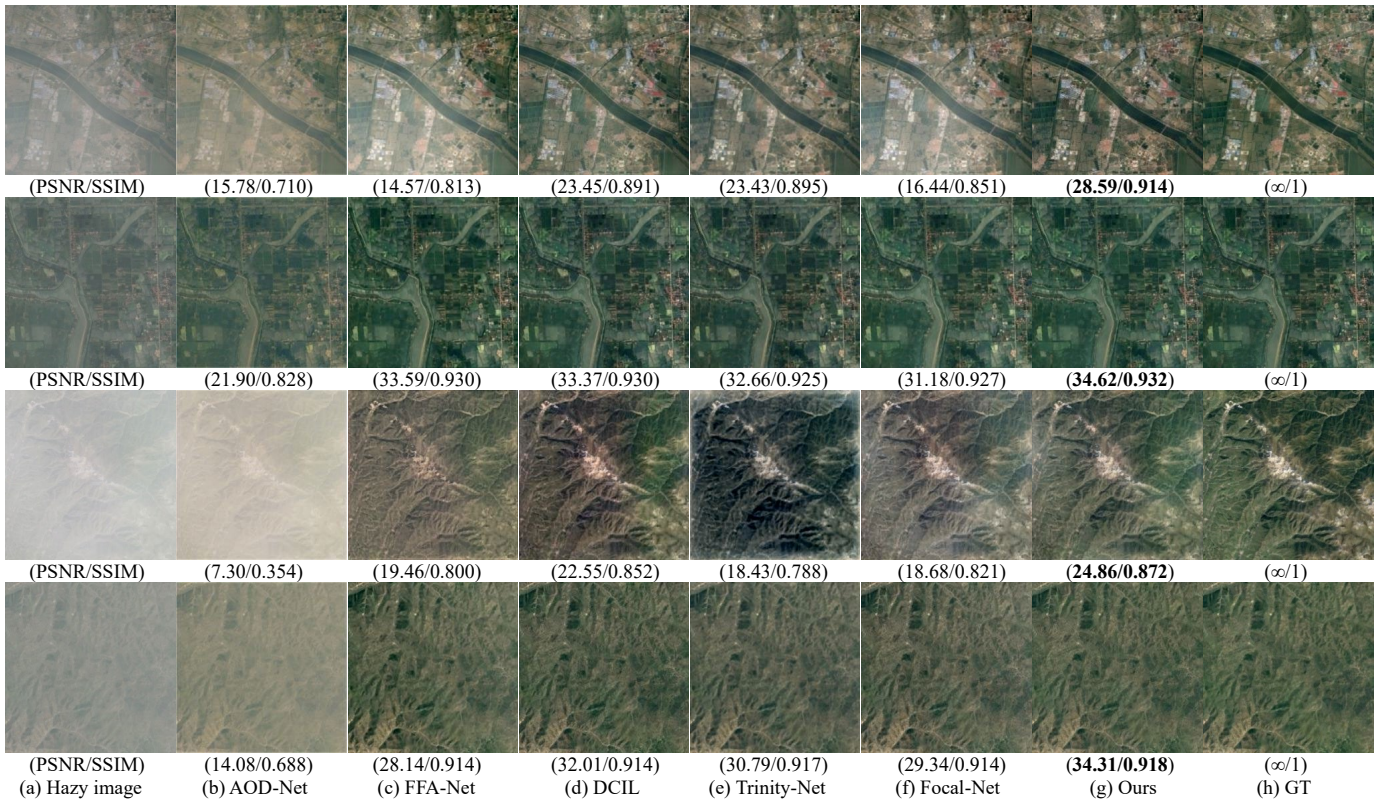


Fig. 6. Qualitative comparisons on the real-world ERICE dataset. From (a) to (h): (a) the hazy image, and the dehazing results of (b) AOD-Net [12], (c) FFA-Net [15], (d) DCIL [19], (e) Trinity-Net [35], (f) Focal-Net [17], (g) our RSHazeDiff, respectively, and (h) the ground-truth image. Our RSHazeDiff can generate more natural images with realistic colors and rich details.

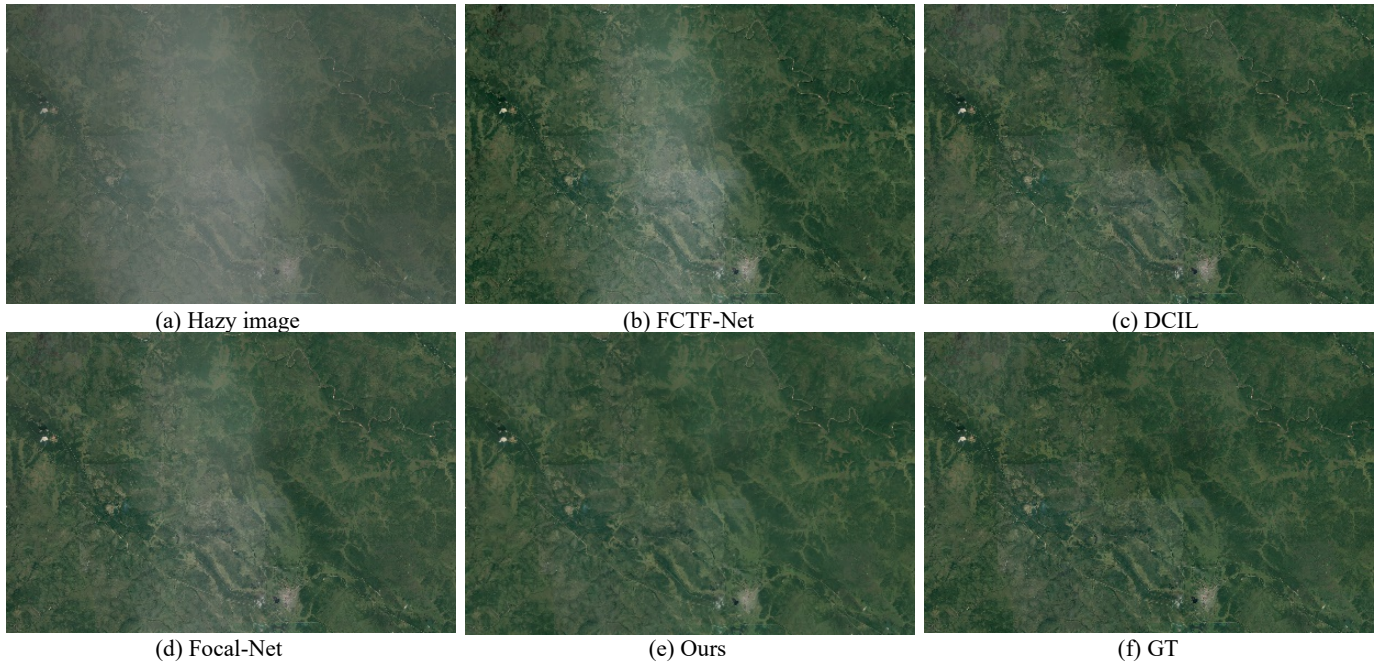


Fig. 7. Dehazing results of different methods on the full-size RICE1 dataset. From (a) to (f): (a) the hazy image with nonuniform haze (3072 × 2048), and the dehazing results of (b) FCTF-Net [18], (c) DCIL [19], (d) Focal-Net [17], (e) our RSHazeDiff, respectively, and (f) the ground-truth image.

TABLE II
AVERAGE PSNR, SSIM AND CIEDE2000 OF VARIOUS DIFFERENT APPROACHES ON THE REAL-WORLD ERICE DATASET. RED AND BLUE COLORS ARE USED TO INDICATE THE 1st AND 2nd RANKS, RESPECTIVELY

Method	Publication	PSNR↑	SSIM↑	CIEDE2000↓
DCP [3]	TPAMI'10	18.13	0.816	11.482
AOD-Net [12]	ICCV'17	20.18	0.807	9.438
GridDehazeNet [14]	ICCV'19	32.73	0.935	2.719
IdERs [6]	INS'19	13.29	0.513	20.701
FFA-Net [15]	AAAI'20	30.81	0.932	3.475
PSD [16]	CVPR'21	26.58	0.918	5.218
FCTF-Net [18]	GRSL'21	33.13	0.933	3.626
DCIL [19]	TGRS'22	35.90	0.942	2.068
Trinity-Net [35]	TGRS'23	30.26	0.942	4.026
Focal-Net [17]	ICCV'23	32.67	0.937	2.691
RSHazeDiff	Ours	36.56	0.958	2.642

in removing the haze of input images completely. Furthermore, our RSHazeDiff can generate visually more pleasing images with faithful colors and richer structural information.

Fig. 7 exhibits the comparison results of different dehazing methods on the full-size RICE1 dataset, with the size of 3072 × 2048. As a display, FCTF-Net has poor ability in handling nonuniform hazy images, leading to abundant haze residual. Focal-Net still cannot remove most of nonuniform haze. The dehazing result of DCIL contains slight haze residual in some regions. In contrast, our RSHazeDiff can remove the nonuniform haze completely.

We also evaluate the dehazing performance of our method on other bands. The hazy samples on RICE2 dataset [57] are composed of three bands, *i.e.*, shortwave infrared 1 (SWIR 1) band, near-infrared (NIR) band, and red band. Fig. 8 shows the dehazing results of our method among the three bands. As observed, RSHazeDiff can produce clear images with rich

structures and few haze residuals.

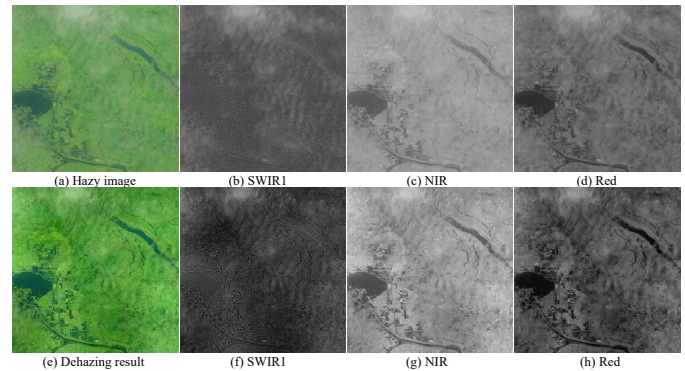


Fig. 8. Dehazing result of each band on RICE2 dataset [57]. From (a) to (d): (a) the hazy image composed by three bands, (b) the shortwave infrared 1 (1.57-1.65 μm), (c) the near-infrared band (0.85-0.88 μm), and (d) the red band (0.64-0.67 μm). (e)-(h) are the dehazing results of (a)-(d), respectively.

C. Analysis of Spectral Consistency

We conduct a spectral consistency analysis to further evaluate the spectral similarity between recovered image and its corresponding ground-truth image in typical land covers. The spectral angle mapper (SAM) [63] index can calculate the spectral similarity between dehazed images \bar{y} and reference images y , which is formulated as:

$$SAM = \frac{1}{P} \sum_{p=1}^P \cos^{-1} \left(\frac{y_p^T \bar{y}_p}{\|y_p\|_2 \cdot \|\bar{y}_p\|_2} \right) \quad (15)$$

where P is the total number of pixels. y_p and \bar{y}_p are the vectors $\in \mathcal{R}^{1 \times C}$ for the pixel p . The C means the number of bands.

A smaller value of SAM indicates higher spectral similarity between dehazed images and reference images.

As exhibited in Fig. 9, we report SAM values of different dehazing methods in some land covers marked by cross 1-4 (e.g., terrace, stream, and soil). As observed, SAM values of haze images among the four land covers are the largest. Compared with other algorithms, our RSHazeDiff achieves the smallest SAM values, which indicates our recovered spectral features of typical land covers are most similar to the ground-truth image.

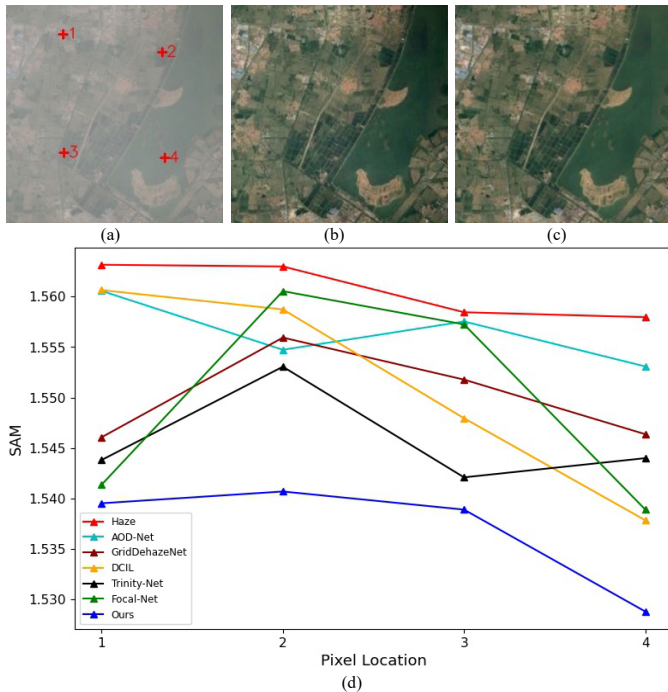


Fig. 9. Spectral profiles of different land covers on ERICE dataset. (a) the hazy image, (b) the dehazing result of our RSHazeDiff, (c) the ground-truth image, and (d) spectral comparison results for the pixels masked by cross 1-4 in the hazy image.

D. Ablation Study

Effect of different components in RSHazeDiff. Our method shows dehazing superiority both quantitatively and qualitatively over eleven representative SOTAs. Furthermore, we perform an ablation study to analyze the effectiveness of the proposed components, including the phased training strategy, Fourier-aware iterative refinement, and global compensated learning module.

We first perform the baseline model with patch-based conditional DDPM and then optimize this model with noise-estimation constraint. Next, key modules are progressively added into the baseline model:

- 1) baseline + phased training strategy $\rightarrow V_1$,
- 2) V_1 + Fourier-aware iterative refinement $\rightarrow V_2$,
- 3) V_2 + global compensated learning module $\rightarrow V_3$ (our full model).

For fair comparisons, all variants are trained in the same way as before and tested on DHID dataset. The performances of these variants can be found in Table III and Fig. 1.

TABLE III
ABLATION STUDY OF DIFFERENT COMPONENTS ON DHID DATASET.

Variants	Baseline	V_1	V_2	V_3
Phased training strategy	w/o	✓	✓	✓
Fourier-aware iterative refinement	w/o	w/o	✓	✓
Global compensated learning module	w/o	w/o	w/o	✓
PSNR	25.50	26.09	26.86	27.91
SSIM	0.878	0.881	0.892	0.900
CIEDE2000	6.176	5.044	4.352	3.945

As shown in Table III and Fig. 1, each component of RSHazeDiff can boost the dehazing performance. When applying the phased training strategy, the model achieves advanced performance that has fewer haze residuals and higher metric values over baseline model. Furthermore, the introduction of FIR and GCL module also have brought performance improvement of model in three indicators. In short, the full model performs favorably against the other variants both quantitatively and qualitatively, demonstrating that all the components of RSHazeDiff are beneficial and necessary for effective haze removal.

Effect of feature fusion module in GCL. Since simple addition or concatenation operations cannot fuse two level features well, we employ two attention modules to enhance the feature fusion capability in a pixel-channel collaborative manner. To explore the performance of different fusion modes in the feature fusion module, we perform an ablation study by setting PA and CA in parallel or in serial, or swapping the addition and concatenation operations. Specifically, one is to adopt the addition/concatenation operation, PA and CA in serial to fuse the outputs of the local patch-based denoising process and GCL module, and the other is to adopt the addition/concatenation operation before PA and the concatenation/addition operation before CA, which are in parallel. As exhibited in Table IV, the feature fusion module can better fuse these two outputs by using our fusion mode.

TABLE IV
ABLATION STUDY OF DIFFERENT FUSION MODES IN THE FEATURE FUSION MODULE.

Fusion Mode	PSNR	SSIM	CIEDE2000
addition PA CA in serial	26.40	0.895	4.312
concatenation PA CA in serial	27.49	0.900	4.243
concatenation PA, addition CA in parallel	27.68	0.899	4.329
addition PA, concatenation CA in parallel (ours)	27.91	0.900	3.945

Effect of sampling steps in sampling process. During the sampling process, diffusion model iteratively denoises until generating sharp results through S steps. Theoretically, a large sampling step contributes to producing more visually pleasing result [29], whereas it also increases the processing time. To further explore the performance of different sampling steps, we perform an ablation experiment setting different S from 5 to 25. Table V exhibits the average PSNR, SSIM and CIEDE2000 of different sampling steps. As reported, we can find that the performance degrades slightly as the number of sampling step is greater than 10. To carefully balance the performance and

sampling time, we set S to 10 in our experiment.

TABLE V
ABLATION STUDY ON THE SAMPLING STEPS IN SAMPLING PROCESS
(HYPERPARAMETER S)

	$S = 5$	$S = 8$	$S = 10$	$S = 12$	$S = 15$	$S = 25$
PSNR	26.38	27.12	27.91	26.97	26.85	27.64
SSIM	0.900	0.902	0.900	0.900	0.897	0.886
CIEDE2000	4.394	4.473	3.945	4.238	4.290	4.552

Effect of the mask scale in FIR. The mask scale (hyperparameter β) is the weight of different amplitude components in FIR. Obviously, when the hyperparameter β is set to 0, the Fourier-aware iterative refinement module is invalid. When β is set to 1, FIR focuses on fusing the phase component of forward process and amplitude component of reverse process in Fourier domain. Table VI shows the dehazing performance of different scale values from 0.01 to 1. As reported, FIR can better help diffusion model to restore haze-free images when the β is set to 0.1.

TABLE VI
ABLATION STUDY ON THE MASK SCALE IN FIR (HYPERPARAMETER β)

	$\beta = 0.01$	$\beta = 0.05$	$\beta = 0.1$	$\beta = 0.5$	$\beta = 1$
PSNR	27.11	27.33	27.91	26.97	27.67
SSIM	0.888	0.887	0.900	0.886	0.890
CIEDE2000	4.963	4.958	3.945	5.188	4.047

VI. CONCLUSION

In this paper, we propose an effective unified Fourier-aware diffusion model for RSID, namely RSHazeDiff. Our work offers a new perspective to tackle image dehazing task, which exploits the generative ability of the conditional DDPM to improve image perceptual quality in dense hazy scenarios. Different from the primitive DDPM, RSHazeDiff performs a fine training phase to pull the sampled dehazed images closer to their corresponding ground-truth counterparts, which can evade the unsatisfactory results caused by simple noise estimation. In addition, we design a Fourier-aware iterative refinement module to help the diffusion model to preserve more realistic colors and richer texture details in the restored image. Furthermore, to mitigate boundary artifacts when processing diffusive patches, a well-designed global compensated learning module is developed to capture the global dependency features of input images. Quantitative and qualitative experiments validate that RSHazeDiff is superior to SOTAs on dense RS image datasets.

Acknowledgements. The authors thank the editors and anonymous reviewers for their careful reading and valuable comments.

REFERENCES

[1] S. Ren and Q. Liu, "Small target augmentation for urban remote sensing image real-time segmentation," *IEEE Transactions on Intelligent Transportation Systems*, 2023.

[2] H. Guan, Y. Yu, D. Li, and H. Wang, "Roadcapsfpn: Capsule feature pyramid network for road extraction from vhr optical remote sensing imagery," *IEEE Transactions on Intelligent Transportation Systems*, vol. 23, no. 8, pp. 11 041–11 051, 2021.

[3] K. He, J. Sun, and X. Tang, "Single image haze removal using dark channel prior," *IEEE Trans. Pattern Anal. Mach. Intell.*, vol. 33, no. 12, pp. 2341–2353, Sep. 2010.

[4] Q. Zhu, J. Mai, and L. Shao, "Single image dehazing using color attenuation prior," in *BMVC*, 2014.

[5] J. Li, Q. Hu, and M. Ai, "Haze and thin cloud removal via sphere model improved dark channel prior," *IEEE Geoscience and Remote Sensing Letters*, vol. 16, no. 3, pp. 472–476, 2018.

[6] L. Xu, D. Zhao, Y. Yan, S. Kwong, J. Chen, and L.-Y. Duan, "Iders: Iterative dehazing method for single remote sensing image," *Information Sciences*, vol. 489, pp. 50–62, 2019.

[7] H. Shen, C. Zhang, H. Li, Q. Yuan, and L. Zhang, "A spatial-spectral adaptive haze removal method for visible remote sensing images," *IEEE Transactions on Geoscience and Remote Sensing*, vol. 58, no. 9, pp. 6168–6180, 2020.

[8] G. Bi, G. Si, Y. Zhao, B. Qi, and H. Lv, "Haze removal for a single remote sensing image using low-rank and sparse prior," *IEEE Transactions on Geoscience and Remote Sensing*, vol. 60, pp. 1–13, 2021.

[9] Y. Han, M. Yin, P. Duan, and P. Ghamisi, "Edge-preserving filtering-based dehazing for remote sensing images," *IEEE Geoscience and Remote Sensing Letters*, vol. 19, pp. 1–5, 2021.

[10] W. Ren, S. Liu, H. Zhang, J. Pan, X. Cao, and M.-H. Yang, "Single image dehazing via multi-scale convolutional neural networks," in *Proc. Eur. Conf. Comput. Vis. (ECCV)*, Oct. 2016, pp. 154–169.

[11] B. Cai, X. Xu, K. Jia, C. Qing, and D. Tao, "Dehazenet: An end-to-end system for single image haze removal," *IEEE transactions on image processing*, vol. 25, no. 11, pp. 5187–5198, 2016.

[12] B. Li, X. Peng, Z. Wang, J. Xu, and D. Feng, "Aod-net: All-in-one dehazing network," in *Proc. IEEE Int. Conf. Comput. Vis. (ICCV)*, Oct. 2017, pp. 4770–4778.

[13] S. G. Narasimhan and S. K. Nayar, "Chromatic framework for vision in bad weather," in *Proc. IEEE/CVF Conf. Comput. Vis. Pattern Recognit. (CVPR)*, vol. 1, Jun. 2000, pp. 598–605.

[14] X. Liu, Y. Ma, Z. Shi, and J. Chen, "Griddehazenet: Attention-based multi-scale network for image dehazing," in *Proceedings of the IEEE/CVF international conference on computer vision*, 2019, pp. 7314–7323.

[15] X. Qin, Z. Wang, Y. Bai, X. Xie, and H. Jia, "Ffa-net: Feature fusion attention network for single image dehazing," in *Proc. AAAI Conf. Artif. Intell. (AAAI)*, vol. 34, no. 07, Feb. 2020, pp. 11 908–11 915.

[16] Z. Chen, Y. Wang, Y. Yang, and D. Liu, "Psd: Principled synthetic-to-real dehazing guided by physical priors," in *Proceedings of the IEEE/CVF conference on computer vision and pattern recognition*, 2021, pp. 7180–7189.

[17] Y. Cui, W. Ren, X. Cao, and A. Knoll, "Focal network for image restoration," in *Proceedings of the IEEE/CVF International Conference on Computer Vision*, 2023, pp. 13 001–13 011.

[18] Y. Li and X. Chen, "A coarse-to-fine two-stage attentive network for haze removal of remote sensing images," *IEEE Geoscience and Remote Sensing Letters*, vol. 18, no. 10, pp. 1751–1755, 2020.

[19] L. Zhang and S. Wang, "Dense haze removal based on dynamic collaborative inference learning for remote sensing images," *IEEE Transactions on Geoscience and Remote Sensing*, vol. 60, pp. 1–16, 2022.

[20] W. Ren, L. Ma, J. Zhang, J. Pan, X. Cao, W. Liu, and M.-H. Yang, "Gated fusion network for single image dehazing," in *Proceedings of the IEEE conference on computer vision and pattern recognition*, 2018, pp. 3253–3261.

[21] H. Zhang and V. M. Patel, "Densely connected pyramid dehazing network," in *Proceedings of the IEEE conference on computer vision and pattern recognition*, 2018, pp. 3194–3203.

[22] D. Engin, A. Genç, and H. Kemal Ekenel, "Cycle-dehaze: Enhanced cyclegan for single image dehazing," in *Proceedings of the IEEE conference on computer vision and pattern recognition workshops*, 2018, pp. 825–833.

[23] Y. Dong, Y. Liu, H. Zhang, S. Chen, and Y. Qiao, "Fd-gan: Generative adversarial networks with fusion-discriminator for single image dehazing," in *Proceedings of the AAAI Conference on Artificial Intelligence*, vol. 34, no. 07, 2020, pp. 10 729–10 736.

[24] Y. Wang, X. Yan, D. Guan, M. Wei, Y. Chen, X.-P. Zhang, and J. Li, "Cycle-snsppan: Towards real-world image dehazing via cycle spectral normalized soft likelihood estimation patch gan," *IEEE Transactions on*

- Intelligent Transportation Systems*, vol. 23, no. 11, pp. 20 368–20 382, 2022.
- [25] Y. Zheng, J. Su, S. Zhang, M. Tao, and L. Wang, “Dehaze-aggan: Unpaired remote sensing image dehazing using enhanced attention-guide generative adversarial networks,” *IEEE Transactions on Geoscience and Remote Sensing*, vol. 60, pp. 1–13, 2022.
- [26] C. Saharia, J. Ho, W. Chan, T. Salimans, D. J. Fleet, and M. Norouzi, “Image super-resolution via iterative refinement,” *IEEE Transactions on Pattern Analysis and Machine Intelligence*, vol. 45, no. 4, pp. 4713–4726, 2022.
- [27] C. Saharia, W. Chan, H. Chang, C. Lee, J. Ho, T. Salimans, D. Fleet, and M. Norouzi, “Palette: Image-to-image diffusion models,” in *ACM SIGGRAPH 2022 Conference Proceedings*, 2022, pp. 1–10.
- [28] L. Guo, C. Wang, W. Yang, S. Huang, Y. Wang, H. Pfister, and B. Wen, “Shadowdiffusion: When degradation prior meets diffusion model for shadow removal,” in *Proceedings of the IEEE/CVF Conference on Computer Vision and Pattern Recognition*, 2023, pp. 14 049–14 058.
- [29] J. Whang, M. Delbracio, H. Talebi, C. Saharia, A. G. Dimakis, and P. Milanfar, “Deblurring via stochastic refinement,” in *Proceedings of the IEEE/CVF Conference on Computer Vision and Pattern Recognition*, 2022, pp. 16 293–16 303.
- [30] J. Ho, A. Jain, and P. Abbeel, “Denoising diffusion probabilistic models,” *Advances in neural information processing systems*, vol. 33, pp. 6840–6851, 2020.
- [31] O. Özdenizci and R. Legenstein, “Restoring vision in adverse weather conditions with patch-based denoising diffusion models,” *IEEE Transactions on Pattern Analysis and Machine Intelligence*, 2023.
- [32] L. Jiao, C. Hu, L. Huo, and P. Tang, “Guided-pix2pix: End-to-end inference and refinement network for image dehazing,” *IEEE Journal of Selected Topics in Applied Earth Observations and Remote Sensing*, vol. 14, pp. 3052–3069, 2021.
- [33] Y. Huang and X. Chen, “Single remote sensing image dehazing using a dual-step cascaded residual dense network,” in *2021 IEEE International Conference on Image Processing (ICIP)*. IEEE, 2021, pp. 3852–3856.
- [34] X. Liu, Z. Shi, Z. Wu, J. Chen, and G. Zhai, “Griddehazenet+: An enhanced multi-scale network with intra-task knowledge transfer for single image dehazing,” *IEEE Transactions on Intelligent Transportation Systems*, vol. 24, no. 1, pp. 870–884, 2022.
- [35] K. Chi, Y. Yuan, and Q. Wang, “Trinity-net: Gradient-guided swin transformer-based remote sensing image dehazing and beyond,” *IEEE Transactions on Geoscience and Remote Sensing*, 2023.
- [36] Y. Wang, J. Xiong, X. Yan, and M. Wei, “Uscformer: unified transformer with semantically contrastive learning for image dehazing,” *IEEE Transactions on Intelligent Transportation Systems*, 2023.
- [37] Z. Liu, Y. Lin, Y. Cao, H. Hu, Y. Wei, Z. Zhang, S. Lin, and B. Guo, “Swin transformer: Hierarchical vision transformer using shifted windows,” in *Proceedings of the IEEE/CVF international conference on computer vision*, 2021, pp. 10 012–10 022.
- [38] J. Sohl-Dickstein, E. Weiss, N. Maheswaranathan, and S. Ganguli, “Deep unsupervised learning using nonequilibrium thermodynamics,” in *International conference on machine learning*. PMLR, 2015, pp. 2256–2265.
- [39] A. Q. Nichol and P. Dhariwal, “Improved denoising diffusion probabilistic models,” in *International Conference on Machine Learning*. PMLR, 2021, pp. 8162–8171.
- [40] R. Rombach, A. Blattmann, D. Lorenz, P. Esser, and B. Ommer, “High-resolution image synthesis with latent diffusion models,” in *Proceedings of the IEEE/CVF conference on computer vision and pattern recognition*, 2022, pp. 10 684–10 695.
- [41] K. Xu, M. Qin, F. Sun, Y. Wang, Y.-K. Chen, and F. Ren, “Learning in the frequency domain,” in *Proceedings of the IEEE/CVF conference on computer vision and pattern recognition*, 2020, pp. 1740–1749.
- [42] L. Chi, B. Jiang, and Y. Mu, “Fast fourier convolution,” *Advances in Neural Information Processing Systems*, vol. 33, pp. 4479–4488, 2020.
- [43] H. Wang, X. Wu, Z. Huang, and E. P. King, “High-frequency component helps explain the generalization of convolutional neural networks,” in *Proceedings of the IEEE/CVF conference on computer vision and pattern recognition*, 2020, pp. 8684–8694.
- [44] M. Zhou, H. Yu, J. Huang, F. Zhao, J. Gu, C. C. Loy, D. Meng, and C. Li, “Deep fourier up-sampling,” *arXiv preprint arXiv:2210.05171*, 2022.
- [45] Y. Yang, D. Lao, G. Sundaramoorthi, and S. Soatto, “Phase consistent ecological domain adaptation,” in *Proceedings of the IEEE/CVF Conference on Computer Vision and Pattern Recognition*, 2020, pp. 9011–9020.
- [46] Y. Yang and S. Soatto, “Fda: Fourier domain adaptation for semantic segmentation,” in *Proceedings of the IEEE/CVF conference on computer vision and pattern recognition*, 2020, pp. 4085–4095.
- [47] D. Fuoli, L. Van Gool, and R. Timofte, “Fourier space losses for efficient perceptual image super-resolution,” in *Proceedings of the IEEE/CVF International Conference on Computer Vision*, 2021, pp. 2360–2369.
- [48] H. Yu, N. Zheng, M. Zhou, J. Huang, Z. Xiao, and F. Zhao, “Frequency and spatial dual guidance for image dehazing,” in *European Conference on Computer Vision*. Springer, 2022, pp. 181–198.
- [49] O. Ronneberger, P. Fischer, and T. Brox, “U-net: Convolutional networks for biomedical image segmentation,” in *Medical Image Computing and Computer-Assisted Intervention—MICCAI 2015: 18th International Conference, Munich, Germany, October 5-9, 2015, Proceedings, Part III 18*. Springer, 2015, pp. 234–241.
- [50] Q. Xu, R. Zhang, Y. Zhang, Y. Wang, and Q. Tian, “A fourier-based framework for domain generalization,” in *Proceedings of the IEEE/CVF Conference on Computer Vision and Pattern Recognition*, 2021, pp. 14 383–14 392.
- [51] E. Prince and E. Prince, “The fast fourier transform,” *Mathematical Techniques in Crystallography and Materials Science*, pp. 140–156, 1994.
- [52] J. I. Richards, “Review: Yitzhak katznelson, an introduction to harmonic analysis,” *Bulletin of the American Mathematical Society*, vol. 75, no. 4, p. 709–713. [Online]. Available: <http://dx.doi.org/10.1090/s0002-9904-1969-12253-6>
- [53] H. Dong, J. Pan, L. Xiang, Z. Hu, X. Zhang, F. Wang, and M.-H. Yang, “Multi-scale boosted dehazing network with dense feature fusion,” in *Proceedings of the IEEE/CVF conference on computer vision and pattern recognition*, 2020, pp. 2157–2167.
- [54] H. Zhao, O. Gallo, I. Frosio, and J. Kautz, “Loss functions for image restoration with neural networks,” *IEEE Transactions on computational imaging*, vol. 3, no. 1, pp. 47–57, 2016.
- [55] Z. Wang, E. P. Simoncelli, and A. C. Bovik, “Multiscale structural similarity for image quality assessment,” in *Proc. 37th Asilomar Conf. Signals, Syst. Comput.*, vol. 2, Nov. 2003, pp. 1398–1402.
- [56] K. Simonyan and A. Zisserman, “Very deep convolutional networks for large-scale image recognition,” *arXiv preprint arXiv:1409.1556*, 2014.
- [57] D. Lin, G. Xu, X. Wang, Y. Wang, X. Sun, and K. Fu, “A remote sensing image dataset for cloud removal,” *arXiv preprint arXiv:1901.00600*, 2019.
- [58] A. Paszke, S. Gross, F. Massa, A. Lerer, J. Bradbury, G. Chanan, T. Killeen, Z. Lin, N. Gimelshein, L. Antiga *et al.*, “Pytorch: An imperative style, high-performance deep learning library,” *Advances in neural information processing systems*, vol. 32, 2019.
- [59] J. Song, C. Meng, and S. Ermon, “Denoising diffusion implicit models,” *arXiv preprint arXiv:2010.02502*, 2020.
- [60] Y. Song and S. Ermon, “Improved techniques for training score-based generative models,” *Advances in neural information processing systems*, vol. 33, pp. 12 438–12 448, 2020.
- [61] I. Q. Assessment, “From error visibility to structural similarity,” *IEEE Trans. Image Process.*, vol. 13, no. 4, p. 93, Apr. 2004.
- [62] G. Sharma, W. Wu, and E. N. Dalal, “The ciede2000 color-difference formula: Implementation notes, supplementary test data, and mathematical observations,” *Color Res. Appl.*, vol. 30, no. 1, pp. 21–30, Dec. 2004.
- [63] R. H. Yuhas, A. F. Goetz, and J. W. Boardman, “Discrimination among semi-arid landscape endmembers using the spectral angle mapper (sam) algorithm,” in *JPL, Summaries of the Third Annual JPL Airborne Geoscience Workshop. Volume 1: AVIRIS Workshop*, 1992.